J. Fluid Mech. (1991), *vol.* 228, *pp.* 417–442
Printed in Great Britain

Numerical calculation of the underwater noise of rain

By HASAN N. OĞUZ AND ANDREA PROSPERETTI
Department of Mechanical Engineering, The Johns Hopkins University, Baltimore, MD 21218, USA

(Received 15 March 1990 and in revised form 31 October 1990)

When raindrops with a diameter of the order of 1 mm hit a plane water surface they entrain air bubbles that radiate noise in the course of volume oscillations. The paper presents a model of the underwater noise of rain produced by this process. The depth of submergence, radius, and initial energy of the entrained bubbles are obtained numerically for a number of drop sizes. The bubbles are assumed to radiate as dipoles, and the total underwater noise is calculated by integrating over the size of the entraining rain drops. The results are compared both with laboratory experiments of single-drop impacts and field data of rain noise. It is found that the model gives somewhat larger bubbles than are observed experimentally. As a consequence, the characteristic spectral peak of rain is predicted to occur at a somewhat lower frequency than found in experiment. However the level of the peak is in reasonable agreement with data. The amount of noise due to the process of drop impact itself is also estimated and found to be several orders of magnitude lower than the data. Therefore, in spite of some deficiencies of the model and of the computational results, the proposed mechanism for the underwater noise of rain is strongly supported by this study.

1. Introduction

The underwater noise produced by rain has recently been measured by a number of groups and in different conditions (Scrimger 1985; Scrimger *et al.* 1987; Scrimger, Evans & Yee 1989; Nystuen 1986; Nystuen & Farmer 1989; Pumphrey, Crum & Bjørnø 1989). A striking finding common to all these studies is the presence of a very prominent and well-defined spectral peak at a frequency of approximately 14 kHz. Quite unexpectedly, the position and general shape of this peak are found to be independent of the rainfall rate, and even of the size distribution of the rain drops. A striking example, from Scrimger *et al.* (1987), is reproduced in figure 1. Figure 1 (*a*) shows the measured raindrop size distributions for two rain events, the underwater noise of which is shown in figure 1 (*b*). It can be seen that the size distributions look very different, while the measured spectra are strikingly alike. Some other examples can be found in Scrimger *et al.* (1987).

In a recent study (Prosperetti, Pumphrey & Crum 1989) we have proposed an explanation for these findings based on the fluid mechanics of the impact of drops on liquid surfaces. The starting point is work by Pumphrey & Crum (1988), Pumphrey *et al.* (1989), Pumphrey & Crum (1990) and Pumphrey & Elmore (1990) which presents conclusive evidence that most of the noise produced by impacting droplets at normal incidence is not actually produced by the impact itself, but by small air bubbles entrained by the impacting drop. A remarkable feature of this process is

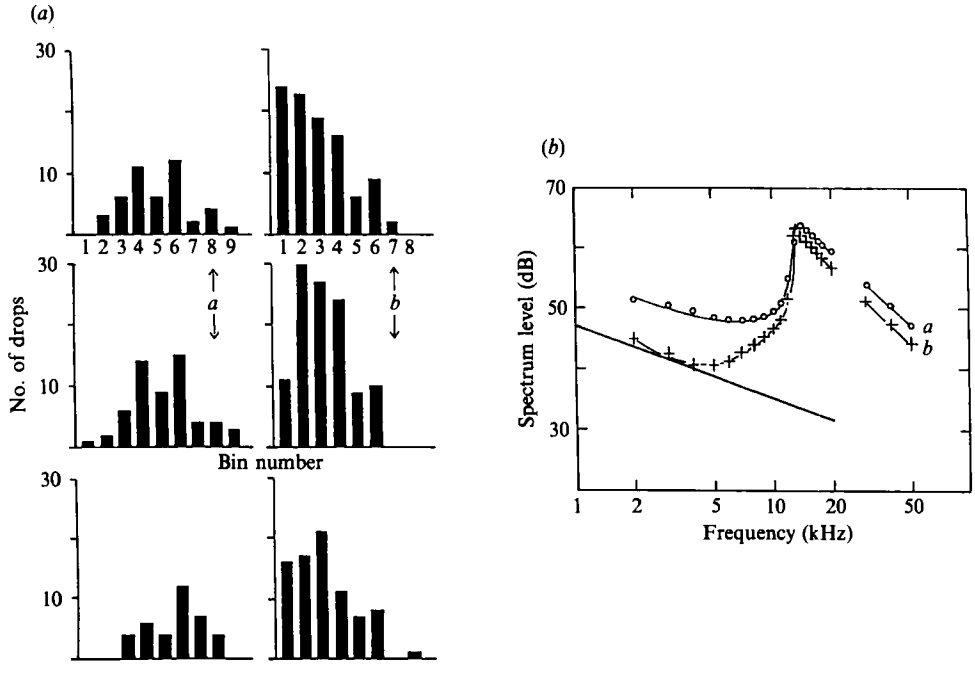

FIGURE 1. (*a*) Measured raindrop size distributions for rain events *a* and *b* of Scrimger *et al.* 1987); (*b*) corresponding underwater noise spectra.

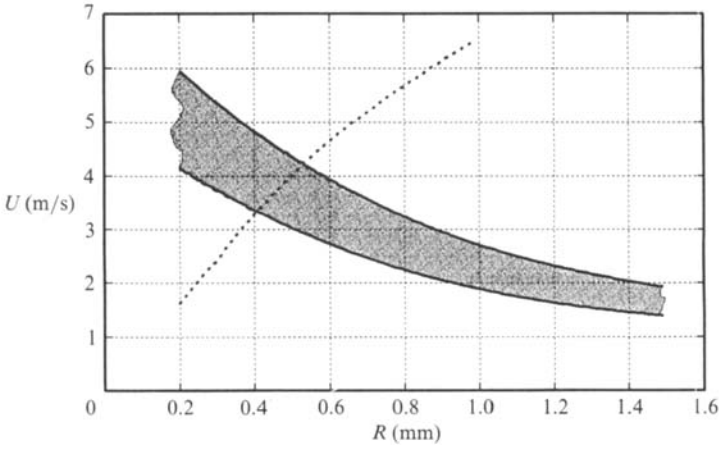

FIGURE 2. The shaded area in the parameter space (R, U) for drop impact represents the regular bubble entrainment region as obtained experimentally by Pumphrey & Crum (1988, 1990). The dotted line is the terminal velocity of a drop in free fall as given by Dingle & Lee (1972).

that, in the parameter space consisting of the drop radius R and impact velocity U, air bubbles are found to be entrained only in a sharply defined region highlighted by the hatching in figure 2. A similar behaviour has been observed in the case of other liquids (Detsch & Harris 1990). While R and U are independent variables in the laboratory or in a computation, in the case of raindrops, they are connected by a functional relation expressing the fact that the drops impact at terminal velocity. This relation is represented by the dotted line on the left of figure 2. The explanation of rain noise put forward in Prosperetti *et al.* (1989) is then that the only drops that make a significant contribution to the underwater noise of rain are those in the

narrowly defined size range where the terminal velocity curve intersects the shaded area in figure 2. Since this range, consisting of drops having radii between 0.47 and 0.55 mm, approximately, is small, some universality may be expected in the acoustic signature of rain. In the case of figure 1 (*a*), the bubble-producing raindrops are those corresponding to bin numbers 6 and 7. It will be observed that, while the overall drop size distributions differ markedly in other size ranges, the drop populations in these bins are fairly similar in both cases, which supports the above explanation.

The purpose of the present paper is to strengthen the plausibility of the rain noise mechanism just described by showing that noise spectra comparable to the experimentally measured ones can be reproduced by completely theoretical means by calculating the size and initial energy of entrained air bubbles, assuming that they radiate as dipoles, and integrating the individual emissions over time and over the surface of the water body. In this way we produce what may be called *synthetic rain-noise spectra*, the only experimental input to which is the raindrop distribution (or, more simply, a total drop count) in the appropriate size range.

From the strictly fluid mechanical viewpoint, the main point of interest of the present work lies in the detailed mechanics of air bubble entrainment and its inhibiting factors at low and high impact velocities. We have already presented a theoretical model and a numerical technique to study this process in an earlier paper (Oğuz & Prosperetti 1990*a*). Here we shall apply that approach to the study of bubble entrainment along the terminal velocity curve of figure 2. A considerable insight into the entrainment mechanics is gained in this way.

2. Rain noise spectrum

In this section we shall show how the underwater noise due to the entrained bubbles can be calculated from a knowledge of the quantities pertaining to the entrainment process.

We assume the surface of the water body on which the rain falls to be flat. This will be true in a time-averaged sense, although the presence of waves may have an important effect on the bubble entrainment, as will be discussed in §6. We also assume that each drop in the narrow regular entrainment region of figure 2 will yield a bubble with an initial energy, radius R_0, and depth of submergence d, all dependent on R.

Since at the time of formation the bubble is not in mechanical equilibrium but has a non-zero energy, this initial energy will be dissipated in the course of the volume pulsations that produce the acoustic emission. The depth of submergence of the entrained bubbles is typically a few millimetres and the wavelength of the sound radiated of the order of 0.1 m. Hence the presence of the neighbouring free surface confers a dipole character to the basically monopole nature of the acoustic radiation. If $p_B(t)$ denotes the pressure on the liquid side of the bubble interface, each bubble will then radiate a pressure field given, far from the bubble, by

$$p = 2d\cos\theta\left(\frac{R_0}{rc}\right)\dot{p}_B\left(t-\frac{r}{c}\right), \tag{1}$$

where R_0 is the radius of the bubble, c the speed of sound in the water, and r and θ are local spherical coordinates with origin at the free surface directly above the bubble, i.e. at the centre of the dipole. Here and in the following the dot denotes differentiation with respect to the argument. The expression (1) does not account for the local deformation of the free surface directly above the entrained bubble. We

have studied this effect in a separate paper (Oğuz & Prosperetti 1990*b*), and found it to be small in the prevailing conditions.

What is usually measured in experiment is the sound spectral level SL defined by

$$SL = 10 \log_{10} \frac{4\pi |\hat{p}_{\mathrm{T}}(x,\omega)|^2}{T[P_{\mathrm{ref}}^2/1\ \mathrm{Hz}]}. \tag{2}$$

Here $\hat{p}_{\mathrm{T}}$ is the time Fourier transform of the (total) acoustic signal p_{T} recorded during a time interval T, and P_{ref} is a conventionally selected reference pressure. Following current usage, we take $P_{\mathrm{ref}} = 1\ \mu\mathrm{Pa}$. The total acoustic field p_{T} contains a contribution p from the oscillating bubbles, a contribution p_{i} due to the impact of the drops, and a contribution p_{b} of background noise. The individual bubble emissions and all of these fields are independent of each other and therefore add incoherently so that

$$|\hat{p}_{\mathrm{T}}|^2 = |\hat{p}|^2 + |\hat{p}_{\mathrm{i}}|^2 + |\hat{p}_{\mathrm{b}}|^2. \tag{3}$$

The calculation of the impact pressure will be described in §5. Here we show how the bubble contribution $\hat{p}$ at a certain position x under the water surface can be obtained. We assume that each surface element $\mathrm{d}S$ is subject to the impact of $n(R)\,\mathrm{d}R\,\mathrm{d}S$ droplets per unit time having a radius between R and $R+\mathrm{d}R$ producing bubbles that radiate incoherently. The sound spectral level at x is then given by the following integral over the water surface and the drop size distribution

$$|\hat{p}(x,\omega)|^2 = T \int_0^{\frac{1}{2}\pi} \mathrm{d}\theta \int_{R_{\mathrm{m}}}^{R_{\mathrm{M}}} \mathrm{d}R\, n \left(\frac{2R_{\mathrm{b}}d}{c}\right)^2 \frac{\cos^2\theta}{r^2} |\hat{p}_{\mathrm{B}}(\omega)|^2 (2\pi \sin\theta) \frac{r^2}{\cos\theta}, \tag{4}$$

where R_{M} and R_{m} are the upper and lower limits of the bubble-entrainment range of drop radii and T is the sampling time. The segment joining x to $\mathrm{d}S$ has length r and forms an angle θ with the vertical. In writing (4) we neglect bottom effects, losses, and non-rectilinear propagation. This equation therefore is applicable only relatively near to the free surface in deep bodies of water. With the assumption of spatial homogeneity of the rain the integration over θ can be carried out with the result

$$|\hat{p}(x,\omega)|^2 = \pi T \int_{R_{\mathrm{m}}}^{R_{\mathrm{M}}} n \left(\frac{R_{\mathrm{b}}d}{c}\right)^2 |\hat{p}_{\mathrm{B}}(\omega)|^2\, \mathrm{d}R. \tag{5}$$

This result is independent of the depth at which the noise level is calculated because of the dipole nature of the surface source distribution. In practice, this independence should be well verified down to depths smaller than the dimensions of the surface area subject to the rain.

In order to carry out the remaining integration over the drop radius R, the dependence on R of the various quantities appearing in the integral (5) must be made explicit. This we shall do with the help of the numerical results for bubble entrainment to be described in §4. Here, we turn our attention to the spectrum $\hat{p}_{\mathrm{B}}$ of the pressure at the bubble surface.

We assume the entrained bubbles to pulsate linearly with a frequency and a damping not very different from those that they would have in an unbounded liquid. This simplification is supported by experiment (Pumphrey 1989; Pumphrey & Crum 1990) and by our theoretical work specifically addressing the effect of a distorted free surface on the oscillations of the bubble (Oğuz & Prosperetti 1990*b*). We write the bubble radius at time t as

$$R_{\mathrm{b}}[1+X(t)], \tag{6}$$

and assume for $X(t)$ the form of a damped sinusoidal oscillation with frequency ω_0,

$$X(t) = X_0 \mathrm{e}^{-bt} \cos(\omega_0 t + \psi), \tag{7}$$

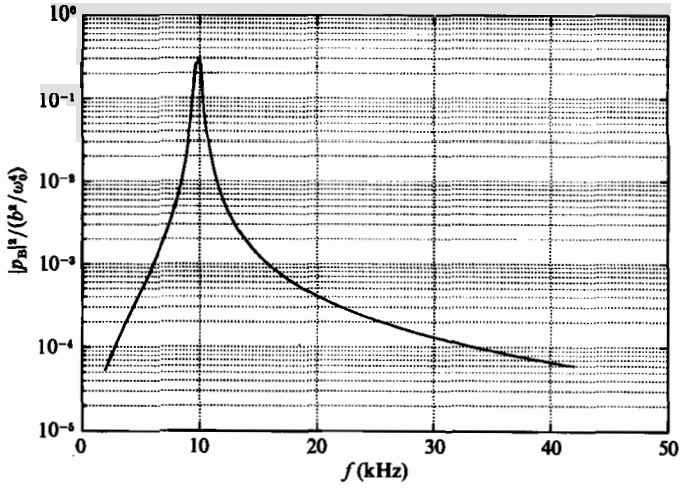

FIGURE 3. Normalized power spectrum of an oscillating bubble according to (11). The graph is a plot of the second fraction in the right-hand side divided by b^2/ω_0^4. The values used for the calculation are $\omega_0 = 61.7 \times 10^3\ \mathrm{s}^{-1}$, $f_0 = 9.8$ kHz, $b = 1.37 \times 10^3\ \mathrm{s}^{-1}$, $\psi = 86.8°$ and correspond to the bubble entrained by a 0.50 mm-radius drop impacting with a terminal velocity of 4.01 m/s.

where b is the damping constant and the amplitude X_0 and phase ψ are given, in terms of the initial conditions $X(0)$, $\dot{X}(0)$ of the bubble motion, by

$$X_0 = \left(X^2(0) + \left[\frac{\dot{X}(0) + bX(0)}{\omega_0}\right]^2\right)^{\frac{1}{2}} \tag{8}$$

and

$$\tan^{-1}\psi = -\frac{\dot{X}(0) + bX(0)}{\omega_0 X(0)}. \tag{9}$$

We shall devote considerable care to the calculation of $X(0)$ and $\dot{X}(0)$ from the numerical results in §4. For $t < 0$, $X(t) = 0$.

In the following b and ω_0 have been calculated from the expressions given in Prosperetti (1984) or (1991). In general the main physical effects causing damping of the oscillations of gas bubbles are heat transfer, viscosity, and sound radiation. Owing to the presence of the free surface, however, the bubbles we are considering loose very little energy due to acoustic radiation and therefore this contribution to b has been neglected. This procedure is supported by the experimental data of Pumphrey & Crum (1990) who measured the damping constant for drop-entrained bubbles and found a better agreement with theory if radiation damping was disregarded.

In terms of the dimensionless oscillation amplitude X the linearized Rayleigh–Plesset equation may be written

$$p_B = p_0 + \rho R_b^2 \ddot{X}, \tag{10}$$

where p_0 is the static pressure and ρ the liquid density. The Fourier transform of $\dot{p}_B$ can then be readily calculated by using (7) and the final result is

$$|\hat{\dot{p}}_B|^2 = \frac{\rho^2 R^4 X_0^2}{4\pi} \frac{(b^2+\omega_0^2)^3 (b^2+\omega_0^2+\omega^2) + A_c \cos 2\psi - A_s \sin 2\psi}{(b^2+\omega_0^2-\omega^2)^2 + 4\omega^2 b^2} \tag{11}$$

where

$$A_s = 4b\omega_0(b^2+\omega_0^2)^2(b^2-\omega_0^2) + 2b\omega^2(3b^4\omega_0 - 10b^2\omega^3 + 3\omega_0^5), \tag{12}$$

$$A_c = (b^2+\omega_0^2)^2(b^4+\omega_0^4-6b^2\omega_0^2) + \omega^2(b^6 - 15b^4\omega_0^2 + 15b^2\omega_0^4 - \omega_0^6).$$

To show the frequency dependence of the result (11) we present in figure 3 a graph of the second fraction in the right-hand side as a function of frequency $f = \omega/2\pi$ for the case of a bubble with a diameter of 0.65 mm with $\psi = 86.78°$. As calculated according to the procedure of §4, these are the appropriate values for a drop with a radius $R = 0.50$ mm impacting at terminal velocity. The very sharp peak is a consequence of the smallness of the damping.

The preceding procedure assumes radial pulsations of the bubbles and therefore neglects distortions of the spherical shape. Whenever, as in the present case, volume pulsations are strongly excited, radiation from the shape modes can be neglected even in the presence of nonlinear resonance.

3. Entrainment dynamics

We now address the task of numerically determining the bubble size and initial conditions that appear in the expression (11) of the radiated pressure power spectrum. For this purpose we make use of a mathematical model and numerical method that have been described in detail in an earlier paper (Oğuz & Prosperetti 1990*a*). Briefly, the model assumes inviscid potential flow and the calculations, carried out by means of a novel formulation of the boundary element method, presuppose normal impact and axial symmetry. These are evidently idealizations of the real physical process. In particular, in the presence of wind and waves, the rain drops may impact at an appreciable angle. We shall comment later on the likely effect of this circumstance that is ignored in the model.

The plan of the calculation is the following. We choose a number of drop radii in the bubble entrainment range. For each one of these values of the radius we calculate the terminal velocity according to Dingle & Lee (1972), and then run our numerical simulation of the impact process. At the end of the simulation we calculate the size and initial energy of the entrained air bubble. In this manner we obtain the functional relationship between R and the quantities appearing in the integrand of (5) at discrete points. By suitably interpolating these values, the integration can be carried out and the spectrum calculated.

Such a plan is rather ambitious and one cannot expect complete success. For example, from a detailed experimental study of drop impact carried out by Pumphrey & Elmore (1990), it is known that bubble entrainment near the boundaries of the entrainment range is not entirely reproducible even in laboratory conditions. A typical example is shown in figure 4, reproduced from that paper. This figure shows the measured frequencies radiated by the entrained bubbles for a drop radius of 0.5 mm and variable impact velocities. Each point is the average of at least 30 drops, and the vertical bars indicate the standard deviation. It can be seen that, near the centre of the entrainment region, the scatter of the data is very small and the process quite reproducible. However, in the neighbourhood of the lower and upper boundaries, large fluctuations arise. These considerations imply that one cannot expect much more than a general agreement between measured and computed spectra.

For a better understanding of the entrainment process, it is of interest to show in broad outline the sequence of events eventually leading to the entrapment of a bubble. For this purpose we include figure 5, corresponding to the case $R = 0.5$ mm, $U = 4.01$ m/s. Aside from small variations, this sequence is typical of all of the air entrainment cases. In the early stages the bottom of the crater tends to be flat. Later, the outward motion of the sides tends to reverse before that of the bottom, which

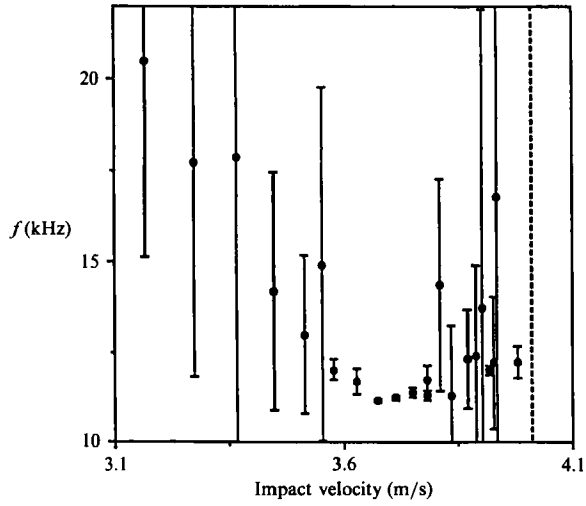

FIGURE 4. Measured frequency of oscillation and standard deviations of the bubble entrapped by the impact of a drop of radius 0.5 mm as a function of the impact velocity U. Each data point is an average of at least 30 impacts (from Pumphrey & Elmore 1990). Drop diameter = 1.00 mm; ●, f (kHz); ---, terminal velocity 4.015 m/s.

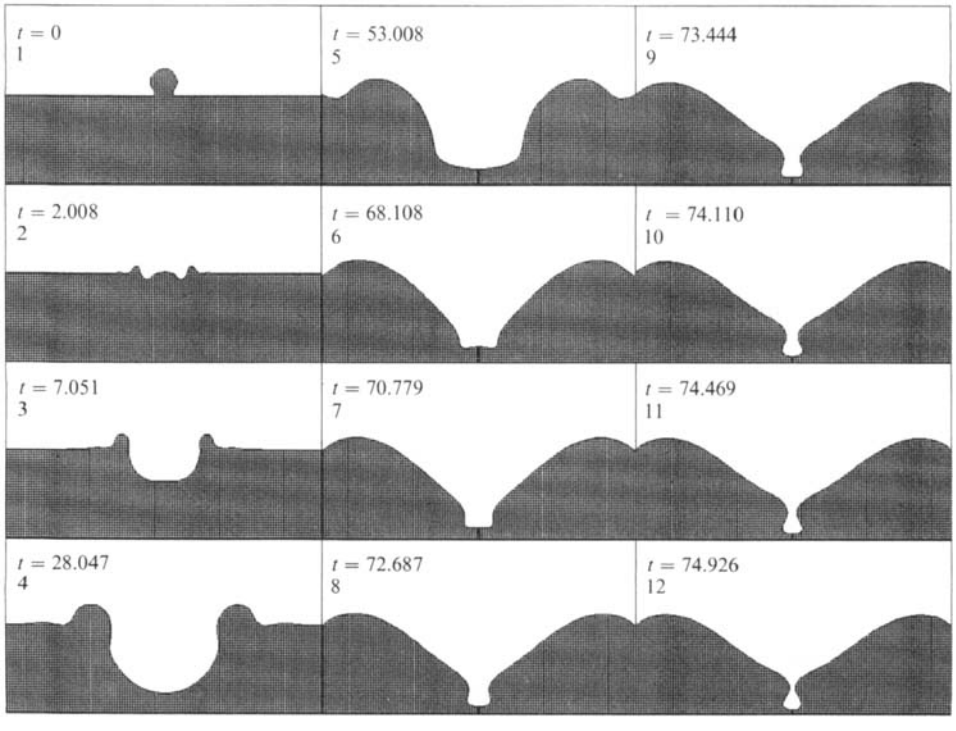

FIGURE 5. Calculated successive free-surface shapes for the case of a 0.5 mm-radius drop impacting a plane liquid surface at the terminal velocity of 4.01 m/s (top to bottom, left to right). The time values indicated are in non-dimensional units referred to R/U. The calculation suggests the entrainment of a bubble 9.35 ms after the impact.

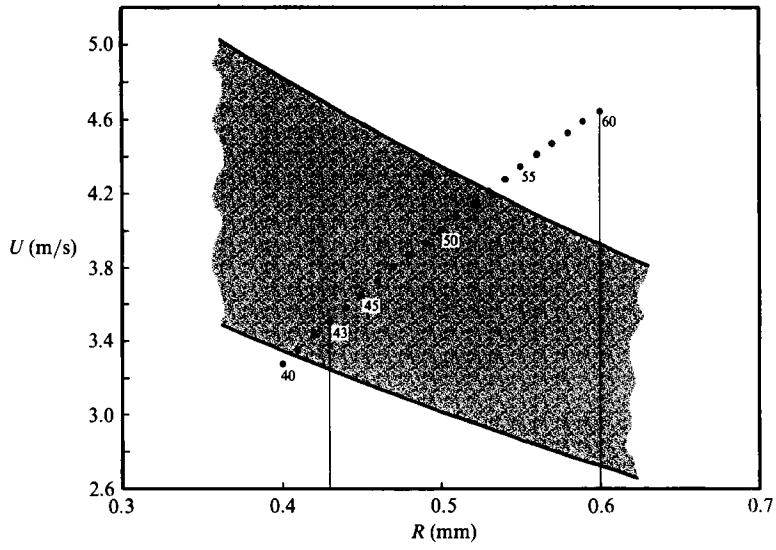

FIGURE 6. Enlargement of the region of the (R, U)-plane of figure 2 near the terminal velocity line. The solid dots represent the cases simulated numerically and the vertical lines the upper and lower limits of bubble entrapment according to the calculations.

leads to a curious funnel shape which is confirmed by experiment (Pumphrey & Crum 1988; Pumphrey *et al.* 1989; Pumphrey 1989; Pumphrey & Crum, 1990; Pumphrey & Elmore 1990). In this stage of the motion the crater is approximately conical, in close agreement with an exact potential-flow solution developed by Longuet-Higgins (1990). According to this solution, the aperture of the cone decreases to a critical value of 109°, at which point a singularity is developed. Our numerical results are consistent with the existence of a limiting angle of this order and with the time evolution of the aperture of the cone predicted by Longuet-Higgins. His basic solution does not, however, include surface tension, which is accounted for only perturbatively. This circumstance suggests that the importance of surface tension is limited to the vicinity of the bottom of the crater, where the bubble is entrapped, but is relatively small elsewhere.

The cases for which the numerical simulations were carried out are shown by the dots along the terminal velocity line in figure 6, which is an enlargement of the corresponding part of figure 2. For convenience the computed points are labelled by a number that expresses the radius of the impacting drop in units of 0.01 mm. Contrary to the experimental limit, somewhere between 0.40 and 0.41 mm, our numerical method does not lead to bubble entrainment for drops smaller than 0.43 mm (i.e. below point 43). A similar disagreement exists for the upper limit, with experiment placing it close to 0.53 mm, but computations still suggesting entrainment for a radius of 0.60 mm. These discrepancies have important consequences on the final results of our computations and will be discussed in §6. For each one of the cases marked in figure 6, we show in figure 7 the free surface shape in the vicinity of the bubble for the last computed timestep.

We have argued in an earlier paper (Oğuz & Prosperetti 1990*c*) that a possible mechanism for the entrapment of a bubble can be found in the capillary wave that, as can be seen in figure 5, originates at the rim of the crater. As this wave progresses inward, it tends to grow owing to geometric focusing and, if it has a sufficient amplitude and a suitable phase, it will eventually overturn and encapsulate a pocket

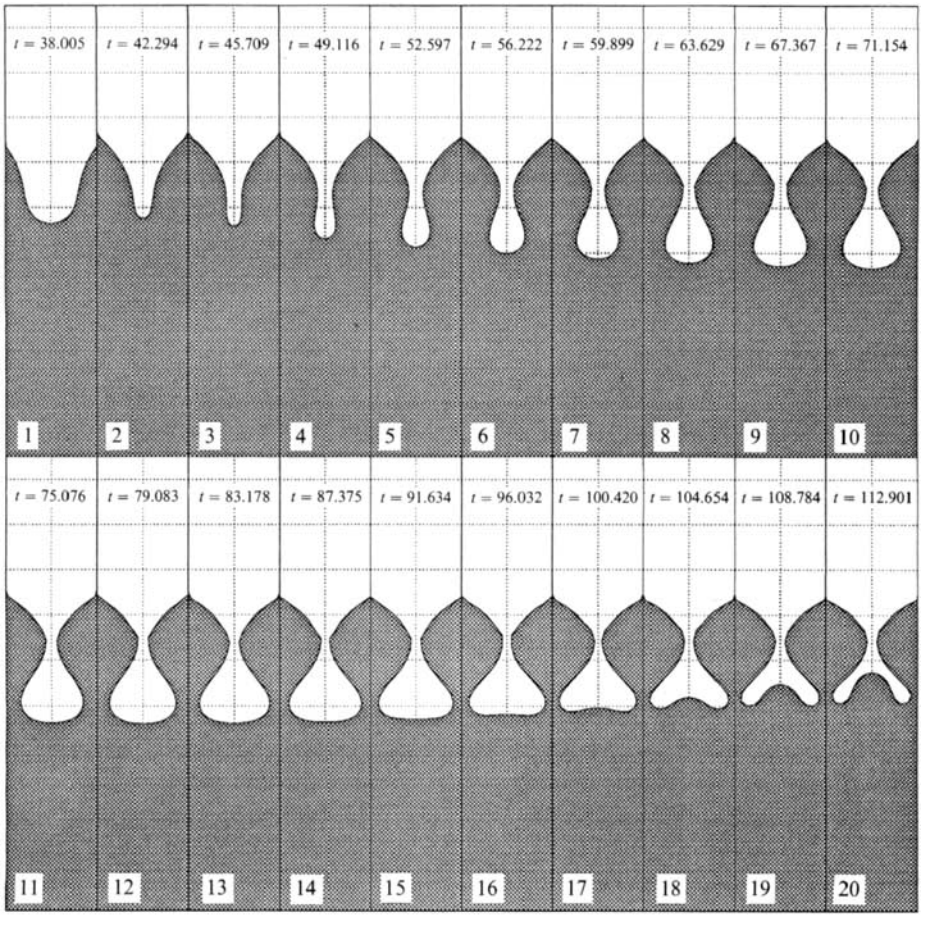

FIGURE 7. Last computed free-surface shapes of the region of the flow where bubbles are entrapped for the cases marked by dots in the previous figure with the corresponding non-dimensional times. The values of the drop radii vary between 0.41 and 0.50 mm in the top line and between 0.51 and 0.60 mm in the bottom line. The radius increment is 0.01 mm. The calculations suggest that bubble entrapment starts at $R = 0.43$ mm.

of air upon reaching the axis of symmetry. For this to happen, the amplitude of the wave and the radius of the crater, both of which are evidently directly related to the energy of the impact, must be sufficiently large. This consideration is compatible with the existence of a lower bound on the velocity of the drop for entrainment to occur. Just above this lower bound, the wave will not have overturned very much, which suggests that the entrained bubble should exhibit a narrow and vertically elongated shape as is indeed seen in the first few examples of figure 7. That, in these conditions, the process is very sensitive to local surface impurities and disturbances is confirmed by the large scatter of the data of figure 4 in the vicinity of the lower entrainment boundary.

As the impact velocity increases, the entrained bubble becomes wider with a much flatter bottom. This is the region in which, as experiment suggests, the entrainment process is very reproducible. We therefore expect our simulations to be more reliable in these cases. At still higher impact velocities, a transition takes place to a regime in which an upward jet, originating at the bottom of the crater, fills most of the cavity before the sides can close in and entrap the air. As the impact velocity is

increased further, this jet develops earlier and earlier with respect to the time of reversal of the outward motion of the crater's sides. Eventually, it shoots out of the crater before the sides can establish contact, thus completely preventing air entrainment. Whether one or many minute bubbles are entrained in such marginal cases as shown in examples 58–60 of figure 7 is not clear. Certainly, according to the experimental data of figure 4, in this regime entrainment is not very reproducible. It may be noted that this trend with increasing velocity is very different from the case of a solid sphere in which bubbles are always entrained provided a minimum impact velocity is exceeded (Richardson 1948, 1955).

4. The entrapped bubble

The input to the noise spectrum calculation of §2 consists of the initial volume, the initial rate of change of the volume, and the initial depth of each entrained bubble as a function of the radius and impact velocity of the entraining droplet. The numerical calculations are carried out in terms of dimensionless variables, indicated by an asterisk, referred to the characteristic length R and time R/U. Differentiation with respect to the dimensionless time is indicated by a prime.

Even though the entrained bubbles appear to be visually well defined, to avoid biasing the results, it is important to implement an algorithm capable of automatically identifying the quantities of interest for each numerical simulation. For this purpose we proceed as follows. After the nipple at the bottom of the crater starts to develop (see e.g. frame 7 for $t_* = 70.779$ of figure 5), for each timestep, we identify the point (actually a circle in the axis-symmetric geometry) closest to the z-axis. We denote the distance of this point from the axis of symmetry (i.e. the radius of the circle) by $r_*(t_*)$ and the portion of the trace of the free surface on a meridian plane below this line by $S_b(t_*)$. For each subsequent time-step we calculate the integrals

$$v_* = \pi \int_{S_b} r_*^2 \frac{\mathrm{d}z_*}{\mathrm{d}s} \mathrm{d}s, \tag{13}$$

$$v_*' = 2\pi \int_{S_b} \frac{\partial \phi_*}{\partial n_*} r_* \mathrm{d}s, \tag{14}$$

$$d_* = \frac{\pi}{v_*} \int_{S_b} r_*^2 z_* \frac{\mathrm{d}z_*}{\mathrm{d}s} \mathrm{d}s, \tag{15}$$

where s is the (dimensionless) arclength along S_b measured from the axis of symmetry and ϕ_* the (dimensionless) velocity potential. At the instant of time at which the bubble closes, these integrals give the initial bubble volume $v_*(0) = v(0)/R^3$, the initial volume velocity $v'(0) = \dot{v}(0)/UR^2$, and the initial depth $d_*(0) = d(0)/R$ below the undisturbed free surface of the centre of the volume of the entrapped gas. In the calculation the surface is defined by points (with cylindrical coordinates r_* and z_*), typically 10 to 15 in the region S_b. To evaluate the integrals all the surface quantities such as r_*, z_*, $\partial\phi_*/\partial n_*$ are fitted by cubic splines for increased accuracy. The 10-node Gauss–Legendre quadrature formula is used over each arc joining two consecutive points along the surface. It should be noted that, since $S_b(t_*)$ is not a material line, one would not expect the integral (14) to equal the time derivative of (13).

The initial volume $v(0)$ is converted to an effective initial radius $R_b(0)$ by using the relation expressing the volume of a sphere. Since the bubble, at closure, contains air at atmospheric pressure, because of surface tension, this effective radius is slightly

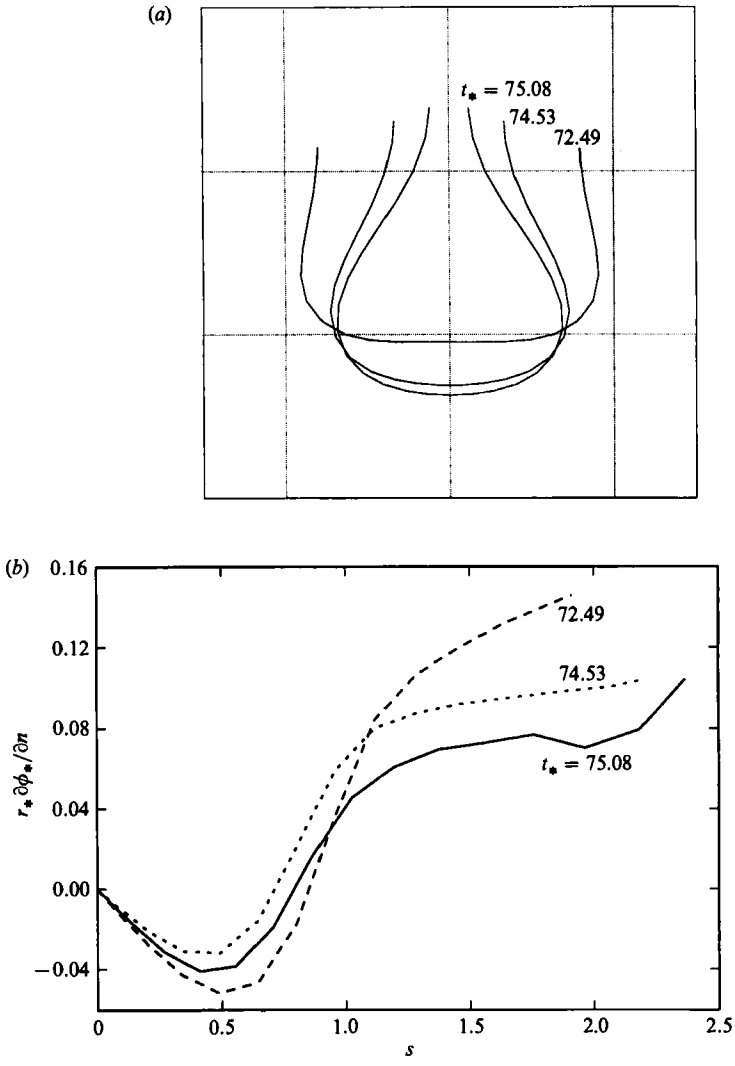

FIGURE 8. (*a*) Three free surface configurations of S_b at $t_* = 72.49$, 74.53, and 75.08 ($R = 0.50$ mm, $U = 4.01$ m/s). (*b*) Graph of $r_* \partial\phi_*/\partial n_*$, the integrand of (14), for the three surface shapes shown in *a*.

larger than the equilibrium radius of the bubble. For the range of bubble radii encountered here, however, the difference is of the order of 0.1% and may be ignored in the calculation of the natural frequency and damping of the oscillations. However, this effect is included in the calculation of the initial displacement $X(0)$ of the oscillator defined in §2 which is obtained from

$$X(0) \approx \frac{2\sigma}{3\kappa p_0 R_b}, \tag{16}$$

where κ is the polytropic exponent (Prosperetti 1984, 1991). The initial velocity $\dot{X}(0)$ is calculated from

$$\dot{X}(0) = \frac{1}{4\pi}\left(\frac{R}{R_b}\right)^3 \frac{U}{R} v'_*. \tag{17}$$

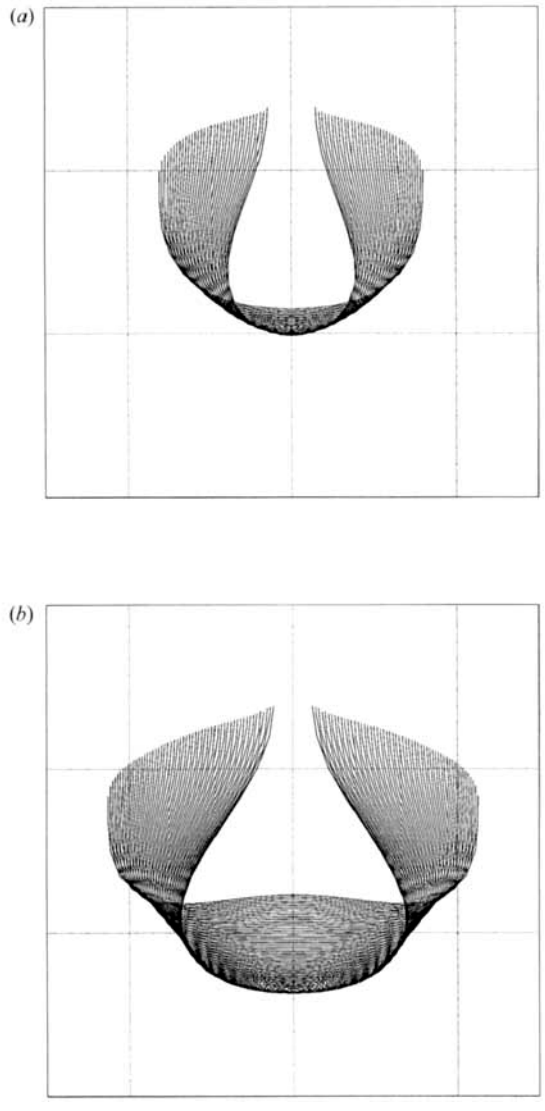

FIGURE 9. (*a*) Sequence of computed surface shapes just before bubble formation for the case $R = 0.45$ mm, $U = 3.66$ m/s. The earliest trace shown is for $t_* = 53.6$ (6.59 ms) and the last one for $t_* = 56.22$ (6.91 ms). (*b*) Sequence of computed surface shapes just before bubble formation for the case $R = 0.5$ mm, $U = 4.01$ m/s. The earliest trace shown is for $t_* = 70.47$ (8.79 ms) and the last one for $t_* = 75.08$ (9.36 ms). The identification of the bubble is explained in the text.

In obtaining these relations the initial energy due to surface tension has been disregarded. It is easy to check from the numerical results to be shown below that this contribution is entirely negligible.

This procedure suffers from several shortcomings that it appears very difficult to obviate. Figure 8(*a*) shows three snapshots of the region $S_b(t_*)$ for $R = 0.5$ mm, $U = 4.01$ m/s at dimensionless times $t_* = 72.49$, 74.54, and 75.08. Figure 8(*b*) shows a graph of the integrand $r_* \partial\phi_*/\partial n_*$ of (14) as a function of the arclength s along the line $S_b(t)$ at the same instant of time. It can be seen that the greatest contribution to the integral comes from the region above the 'equator' of the entrained bubble where the normal velocities are large, even though the distance from the axis is

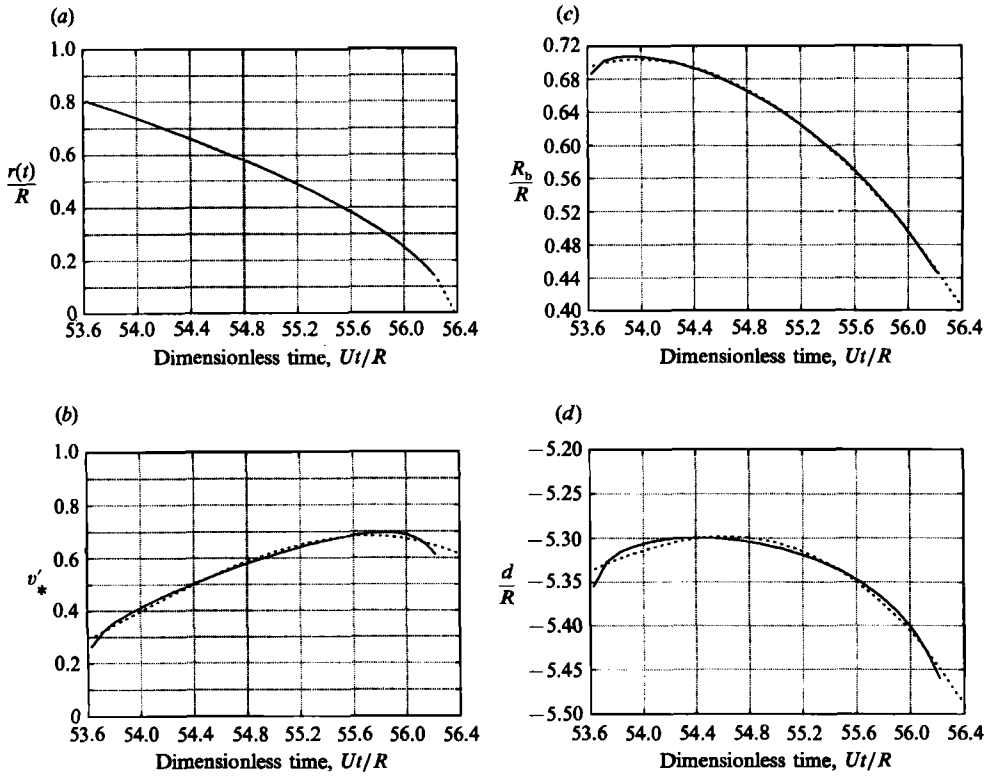

FIGURE 10. Illustration of the extrapolation procedure used for the calculation of the radius, volume rate of change, and depth of submergence of the bubble at the moment of closure for the case $R = 0.45$ mm, $U = 3.66$ m/s. The solid lines are the numerical results and the dashed lines least squares fits. The abscissa is the dimensionless time Ut/R. (*a*) Radius of the bubble's 'neck' r_*. The dotted line is obtained from the least square fit to the computed results (solid line) of an expression of the form const. $\times (t_c - t_*)^{\alpha}$. (*b*) Dimensionless volume rate of change v'_* defined by (14). (*c*) Normalized radius of a sphere having the same volume as computed from (13). This quantity is assumed to be the radius of the entrained bubble at the moment of closure. (*d*) Normalized depth of the entrained bubble, d/R, according to the definition (15).

relatively small. This circumstance causes problems of a physical and computational nature. Just before closure of the cavity, viscous effects in the water and in the air flow become important. Secondly, at the moment of closure, additional energy must be dissipated in a very high-frequency acoustic radiation and, possibly, in local microscopic flows. All these effects will dissipate unknown amounts of the kinetic energy localized in this region. Computationally, a loss of accuracy is possible when the arcs used in the boundary integral method lie very close to the axis of symmetry. Although, of course, the resulting error will have effects everywhere on the free surface, it is expected to be greatest in this high-velocity region near the axis.

Little can be done about the error introduced by the physical processes ignored in the present model. To mitigate the numerical error we follow the time history of the three quantities defined by (13)–(15) for the last 40–50 timesteps of the simulation and extrapolate the result to the instant t_c of closure of the cavity. Typical examples of the procedure can be illustrated with the help of figures 9 and 10. Figures 9(*a*) and 9(*b*) show the portion $S_b(t_*)$ of the free surface over which the integrals (13)–(15) are calculated at different instants of time for the cases $R = 0.45$ mm, $U = 3.66$ m/s and

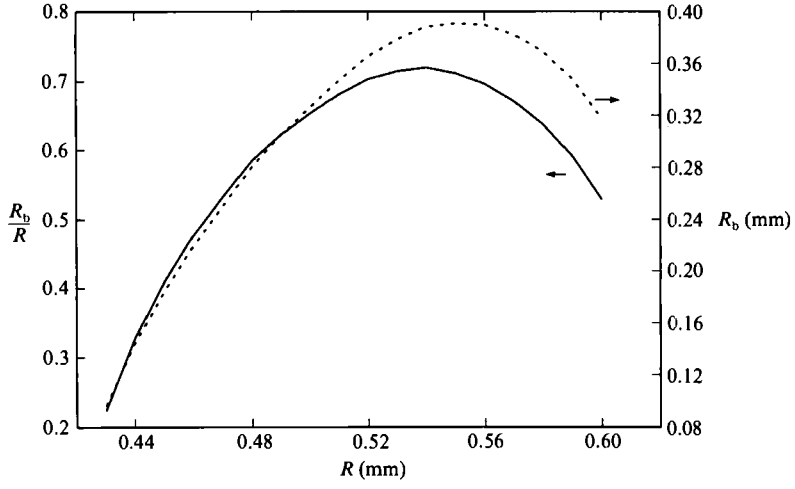

FIGURE 11. The ratio R_b/R (solid line, left-hand vertical scale) and the dimensional bubble radius R_b (dashed line, right-hand vertical scale) at the moment of bubble pinch-off as a function of the radius R of the impacting drop in mm.

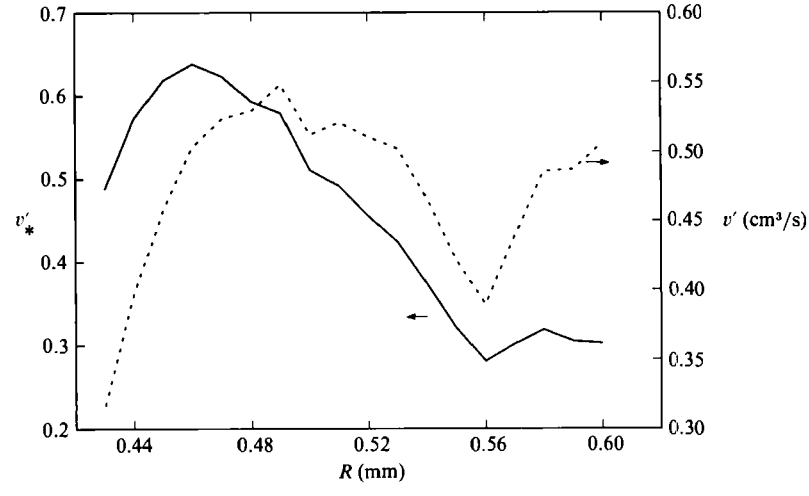

FIGURE 12. Dimensional (dashed line, right-hand vertical scale) and non-dimensional (solid line, left-hand vertical scale) rate of change of the bubble volume at the moment of pinch-off as a function of the radius R of the impacting drop in mm.

$R = 0.5$ mm, $U = 4.01$ m/s. To estimate the instant of closure of the cavity t_c we plot the distance $r_*(t_*)$ of the closest point to the axis as a function of time and extrapolate to $r_* = 0$ by fitting an expression of the type const. $\times (t_c - t_*)^\alpha$. As figure 10(*a*) (corresponding to the case of figure 9*a*) shows, this fit agrees very well with the computed results. Typical values of α are in the range 0.57–0.65.

Knowing t_c, we can proceed to the calculation of the bubble conditions at closure by a similar extrapolation procedure. For the initial equivalent radius and depth of submergence we use extrapolation to t_c based on the least-square fitting of a cubic polynomial to the last computed values of these quantities. Figures 10(*b*)–(*d*) illustrate the accuracy of this procedure for $v'_*(0)$, R_{b*}, and $d_*(0)$ for the case of figure 9(*a*). It is clear that the first quantity, contrary to the other two, is rather sensitive

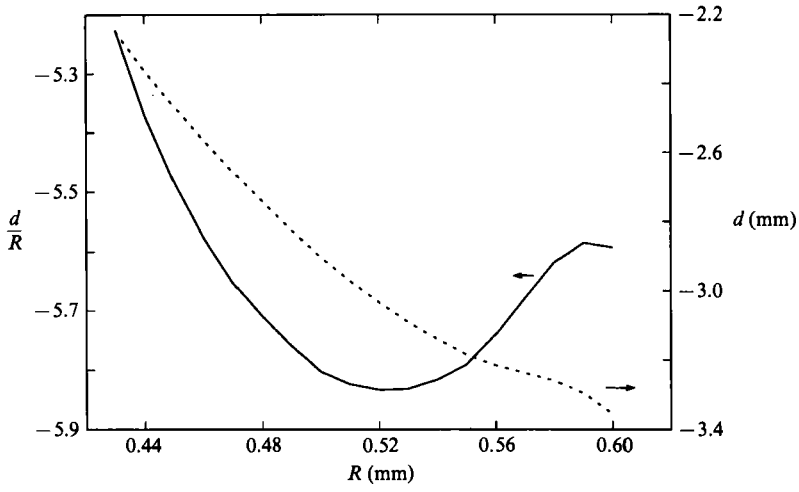

FIGURE 13. Dimensional (dashed line, right-hand vertical scale) and non-dimensional (solid line, left-hand vertical scale) depth d of the entrained bubble at the time of pinch-off as a function of the radius R of the impacting drop in mm.

to this extrapolation. It is interesting to note from figure 10(d) that the bubble is predicted to have a downward acceleration at the moment of closure in agreement with experiment.

By repeating the above procedure for cases 43–60 shown in figures 6 and 7, we obtain R_{b*}, v'_* and d_* as a function of the radius of the impacting drop. The results are plotted in figures 11–13. From these quantities we calculate X_0 and ψ, which are shown in figures 14 and 15 respectively. In these figures, shape-preserving Akima splines are used to interpolate between the computed points. The initial phase of the motion is very close to $\frac{1}{2}\pi$, which implies that the initial energy of the bubbles is mostly kinetic rather than potential. The initial displacement is relatively large for the smaller drops, but they are produced in smaller numbers (figure 15) than the larger ones and do not affect the spectrum of the rain noise very much.

The predictions of this part of our work can be compared with experimental data obtained by Pumphrey & Crum (1990) and Pumphrey & Elmore (1990) for the number of bubbles $N(f)$ entrained per unit frequency increment and for the dipole strength D of the (initial) bubble oscillations. To calculate the first quantity we assume that the number of bubbles in each 1 kHz-interval is proportional to the number of drops entraining bubbles with natural frequency in that range, and that the drops have a uniform distribution in the size range of interest. The proportionality constant is adjusted by matching with the experimental point at the frequency of 10 kHz. The result of this calculation is shown in figure 15 by the dashed line, while the solid line shows the experimental data of Pumphrey & Crum (1990) and Pumphrey & Elmore (1990). Since the scale is bi-logarithmic, the differences are somewhat greater than they appear to be at first sight, but the general trend of the results is quite close, with N decaying approximately proportionally to f^{-3}. It may also be noted that the number of bubbles oscillating at high frequency is several orders of magnitude smaller than that of bigger bubbles.

The dipole moment D is defined by writing the radiated pressure field in the form

$$p = \frac{D}{r}\cos\theta\, \mathrm{e}^{-b\tau}\cos(\omega_0\tau + \psi), \tag{18}$$

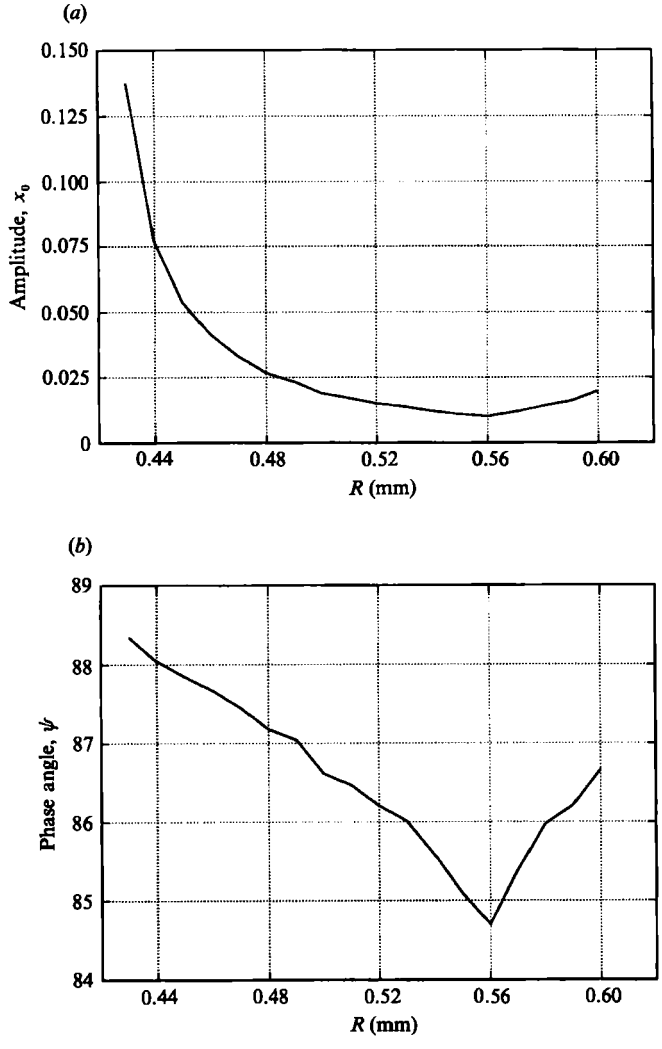

FIGURE 14. (*a*) The computed initial amplitude X_0 of the bubble oscillations as a function of the radius R of the impacting drop. (*b*) The computed phase angle ψ of the bubble oscillations, (7), as a function of the radius R of the impacting drop.

where $\tau = t - r/c$. In view of (1) and (10) D is found to be

$$D = \frac{2\rho d R_0^3}{c} X_0 [\omega_0(\omega_0^2 - 3b^2)\sin\psi + b(3\omega_0^2 - b^2)\cos\psi]. \tag{19}$$

Neglecting for simplicity the initial radius increase of the bubble, so that from (9) $\psi \approx \frac{1}{2}\pi$, and using the fact that $b \ll \omega_0$, from (11) and (8) we readily find the approximate expression

$$D = \frac{d\rho\omega_0^2}{2\pi c}\dot{v}. \tag{20}$$

The dipole moment D obtained from our numerical results according to the previous expression (19) is shown in figure 16 by the dotted line. The points along this line

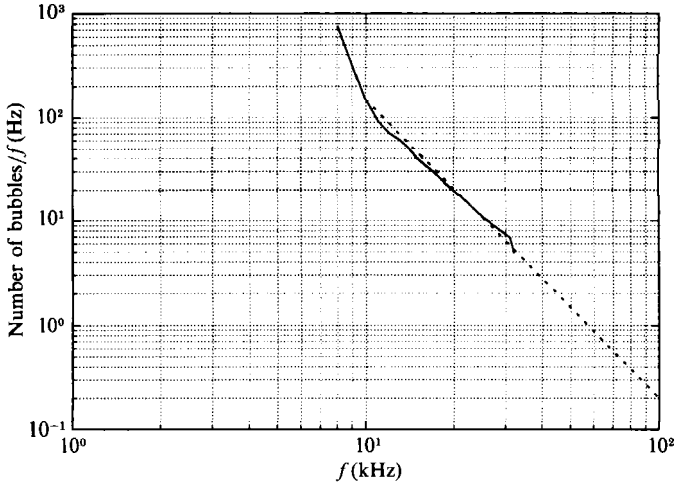

FIGURE 15. Bubble number as a function of their natural frequency in kHz. The vertical axis represents the number of bubbles with a natural frequency within a 1 kHz interval. The distribution of the drops in the radius range between 0.4 and 0.6 mm is assumed to be uniform and the resulting number of bubbles that falls within each 1 kHz interval is evaluated. Experimental distribution obtained by Pumphrey & Crum (1990).

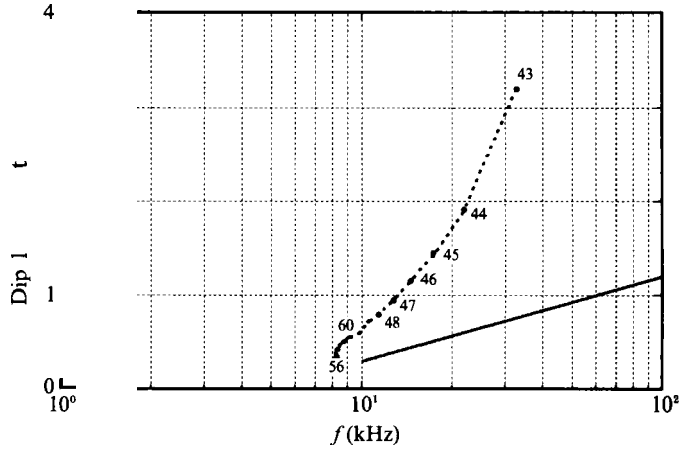

FIGURE 16. The dipole strength D in N/m of the bubbles at the moment of pinch-off as a function of their natural frequency in kHz. The dots along the curve indicate the corresponding impacting drop size in units of 0.01 mm. Note that D is not monotonic with drop size. ——, Experimental results of Pumphrey & Elmore (1990).

correspond to simulations 43–60 of figure 6. The solid line reproduces the measurements of Pumphrey & Crum (1990) and Pumphrey & Elmore (1990). The two sets of results are close for the lower values of D, but diverge markedly at the higher values. These larger values, however, correspond to very small bubbles for which our numerical method is not very precise and which, in any case, contribute very little to the predicted noise level as noted above. The most important difference between data and computation is the fact that the theoretical results extend to lower frequencies than the experimental ones. This is another symptom of the most serious problem affecting our calculation to which we shall return in §6.

Before we can compare field measurements of rain noise with the numerical model, it is necessary to consider the contribution of the drop impact process.

5. Impact noise

Before a bubble is entrapped, the drop impact process itself generates an acoustic field p_i in the water. To estimate this impact noise we proceed as follows.

One can expect the impact noise to be mostly contained in the frequency band $U/R < f < c/R$. These limits follow from the presence of a fast timescale, associated with acoustic propagation in the drop, and a slow timescale, associated with the penetration of the drop into the receiving liquid. It also follows from elementary considerations that the pressure due to the impact must be of the order of

$$p_i \approx \frac{\cos\theta}{r}\frac{R}{\lambda}\frac{U}{R}(\rho U R^2). \tag{21}$$

This form is obtained by likening the impacting drop to a source of mass of magnitude $\rho U R^2$ and by dividing by the timescale R/U in place of taking the time derivative of the source strength. The first factor is the spatial dependence of a dipole source, and the ratio R/λ of the drop radius to the acoustic wavelength is needed to convert monopole to dipole radiation. Here we have assumed the effective depth of the source to be of the order of the only lengthscale available, namely R. Furthermore, consistent with the estimate U/R of the time derivative, we take $\lambda \approx (c/U)R$. The remaining details of the acoustic emission due to the impact must be characterized by a dimensionless function u dependent on time and the only available parameters of the problem R, U, c, ρ. Gravity and surface tension should not appear in this list because they are irrelevant over the short timescales of the impact process. The only possibility for such a function is clearly

$$u = u\left(\frac{Ut}{R}, \frac{U}{c}\right). \tag{22}$$

Since the impact Mach number U/c is very small, dependence on this quantity may be omitted (i.e. U/c can be approximately replaced by 0), and we are led to postulate the following expression for the radiated sound pressure field

$$p_i = \frac{\rho U^3 R}{c} u\left(\frac{Ut}{R}\right)\frac{\cos\theta}{r}. \tag{23}$$

The total energy radiated by the impact is given by

$$E = \int_0^\infty \mathrm{d}t \int_A \mathrm{d}A \frac{p_i^2}{\rho c}, \tag{24}$$

where the integration is extended over any surface completely enclosing the source. By taking this surface to be a sphere centred at the impact point and by neglecting any sound radiated in the air we then find, from (23)

$$E = \frac{2\pi}{3}\left(\frac{\rho R U^3}{c}\right)^2 \frac{1}{\rho c}\int_0^\infty u^2\left(\frac{Ut}{R}\right)\mathrm{d}t, \tag{25}$$

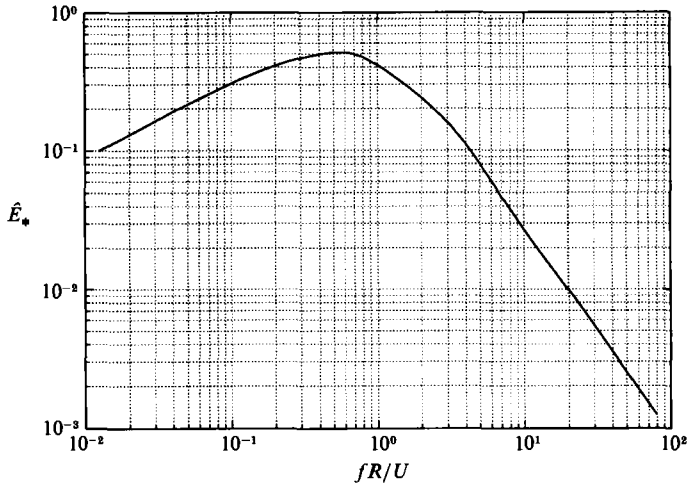

FIGURE 17. The universal impact noise curve (29) according to Franz (1959).

from which, using Parseval's theorem and the fact that the integrand is an even function of ω,

$$E = \frac{4\pi}{3\rho c}\left(\frac{\rho R U^3}{c}\right)^2\left(\frac{R}{U}\right)^2 \int_0^\infty \left|\hat{u}\left(\frac{\omega R}{U}\right)\right|^2 \mathrm{d}\omega, \tag{26}$$

where $\hat{u}$ is the (dimensionless) Fourier transform of the function u defined by

$$\hat{u}(\Omega) = \frac{1}{(2\pi)^{\frac{1}{2}}}\int_{-\infty}^{\infty} u(\tau)\mathrm{e}^{\mathrm{i}\Omega\tau}\,\mathrm{d}\tau. \tag{27}$$

In this relation Ω and τ are conjugate dimensionless variables. The energy density $\hat{E}(f)$ in the frequency band between f and $f+\mathrm{d}f$ can be read directly from (26) and is

$$\hat{E}(f) = 4\pi\frac{R}{U}KM^3\left|\hat{u}\left(\frac{fR}{U}\right)\right|^2, \tag{28}$$

where $K = \frac{2}{3}\pi\rho R^3U^2$ is the kinetic energy of the impacting drop and $M = U/c$ the Mach number of the impact. This argument leads one to expect that the function

$$\hat{E}_*(f_*) \equiv 4\pi\left|\hat{u}\left(\frac{fR}{U}\right)\right|^2 = \frac{U\hat{E}(f)}{RKM^3}, \tag{29}$$

where $f_* = fR/U$, should be a universal function. Indeed Franz (1959) has plotted his measurements of $\hat{E}$ in such a scaled form and has found data falling on a single line when allowance is made for experimental scatter. His results for $\hat{E}$ are summarized in figure 17.

The above equation gives the spectrum for a single drop impacting a liquid surface. To obtain a pressure power spectrum for a given distribution of drop sizes we need to integrate over all the possible sizes and the area. An analysis very similar to the one developed for the bubble noise in §2 leads to the following expression for the sound spectrum level

$$|\hat{p}_1(x,\omega)|^2 = \tfrac{1}{2}T\int_0^\infty \left(\frac{\rho R^2U^2}{c}\right)^2 n\hat{E}_*(f_*)\,\mathrm{d}R, \tag{30}$$

where, as before, n is the number of drops per unit radius increment per unit time per unit area and T is the sampling time. With this expression, the universal curve for the impact spectrum ($\hat{E}_*$) available from Franz's paper, and the knowledge of the drop size distribution for a particular rain event, the portion of rain noise due to drop impact can be calculated.

6. Comparison with experiment

The information presented in figures 11–14, together with known expressions for the damping constant and oscillation frequency of gas bubbles (Prosperetti 1984, 1991), enables us to make a definite prediction of the contribution of bubble entrainment to rain noise provided the number of rain drops falling per unit time, unit surface, and unit radius increment is given. By adding the measured background noise and the noise due to impacts, we are then in a position to compare our theory with experiment and test the hypothesis that most of the underwater noise of rain in the range between 7–8 kHz and 20 kHz is due to the entrained air bubbles.

The only data suitable for our purposes are those by Scrimger *et al.* (1987), who measured both noise levels and rain drop distributions. These data concern five different rain events over a lake, labelled *a*–*e*, in light wind conditions. The drop size distributions were obtained by means of a distrometer. We have already shown in figure 2(*a*) an example of these data as reported in Scrimger *et al.* for events *a* and *b*. We have linearly interpolated and replotted these data in figure 18 for events *a* and *b*, for which the wind speed was 0.9 m/s, and events *c*–*e*, for which the wind speed was 1.4 m/s. This figure shows very different drop size distributions and rainfall intensities and we may therefore conclude that these five data sets are suitable for a test of the present model. The data of Scrimger *et al.* also include the background noise level, common to all five events. These data have been used for $|\hat{p}_b|^2$ in (3).

A comparison between the measured spectra (dotted lines) and our numerically computed 'synthetic' spectra (solid lines) is given in figure 19(*a*–*e*). In view of the poor resolution of the distrometer data in the small range of drop radii where bubbles are entrained, in carrying out the integration over drop size in (5), we have taken n to be a constant. The values used are $n = 575, 325, 299, 284, 284$ number of drops per m^2 per second per mm radius for events *a*–*e* respectively. These numbers have been obtained by adding the number of drops in bins 6 and 7 and dividing by the area (50 cm^2), the duration of the measurement (90 s) and the radius increment (0.2 mm).

Two general conclusions are immediately apparent. The theoretical predictions are in reasonable agreement with the shape of the experimental spectral peak and its level, particularly for rain events *a* and *b*. However, the position of the spectral peak is predicted to be to the left of the experimental one. This suggests that a systematic error is present in our model which produces relatively big bubbles in greater numbers than the actual physical process. An early indication of this problem was furnished by the failure shown in figure 6 of the computed entrainment boundaries to match precisely the experimental ones. The computational entrainment region extends to higher impact velocities and drop radii. It is therefore not surprising to find entrained bubbles with a somewhat larger radius than in the experiment.

It is difficult to pinpoint with precision the source of these discrepancies. For one thing, the large experimental scatter in the results of Pumphrey & Elmore (1990) shown in figure 4 indicates that, especially near the edges of the entrainment region, bubble entrainment is a random process even in laboratory conditions. This evidently highlights the sensitivity of the physical process to even small fluctuations

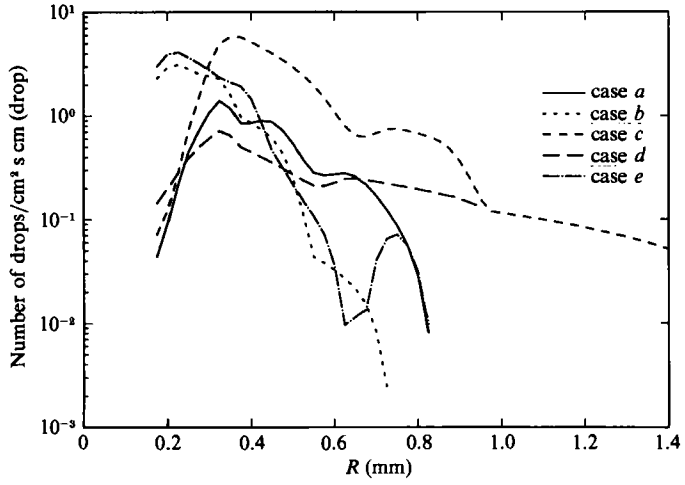

FIGURE 18. The number of drops per unit area (in cm^2), per unit time (in s), per unit radius increment (in cm) as a function of rain drop radius for rain events *a–e* of Scrimger *et al.* (1987).

in the conditions prevailing when it occurs. This sensitivity must of course be mirrored by a corresponding strong effect of small errors on the computed results. As explained in detail in our earlier paper (Oğuz & Prosperetti 1990*a*), the drop impact calculation tends to be very unstable because of surface tension effects. The method that we have developed to handle this problem appears to work quite well for the description of the flow produced by the impacting drop but may lead to some inaccuracies in the calculation of the entrapped bubble which is an event occurring in a very small region of the overall flow. Another problem that is encountered in the calculation is the modelling of the very early stages of the liquid–liquid contact (Oğuz & Prosperetti 1990*a*). Here we have proceeded as in our earlier paper, starting with a finite contact area equal in all cases, and this may introduce some additional error dependent on the radius and velocity of the impacting drop.

A further potential source of error is the neglect of several physical processes. For example, the computational model is based on the assumption of inviscid irrotational flow. While this approximation appears to be justified for the overall flow caused by the drop impact, it may be an oversimplification at particular locations and times. For instance, when the 'neck' of the cavity is about to close, viscous effects in its neighbourhood must become important retarding the formation of the bubble. The liquid at the bottom of the cavity may then have time to rise more than we predict, leading to the entrapment of a smaller volume of air. The air viscosity will have the opposite effect, tending to increase the air pressure in the cavity just before closure.

In the model it has been assumed that each drop falls on a quiescent plane liquid surface. This is certainly an idealization because of the small ripples produced by the other drops, the presence of surface waves, and the effect of the wind that imparts a horizontal component to the velocity of the drops. Evidence that these factors must be important is furnished by a comparison of the experimental spectra for events *a* and *b*, corresponding to light rain and low wind velocity, with those of events *c* and *e*, for which the wind speed was somewhat higher and the rainfall rate much greater. The shape of the peak appears to be fairly sharp in the first two cases, while it is more rounded in the other two. Rain noise data taken at sea in the presence of higher winds (Scrimger *et al.* 1989; Nystuen 1990) also show a broad peak. It is

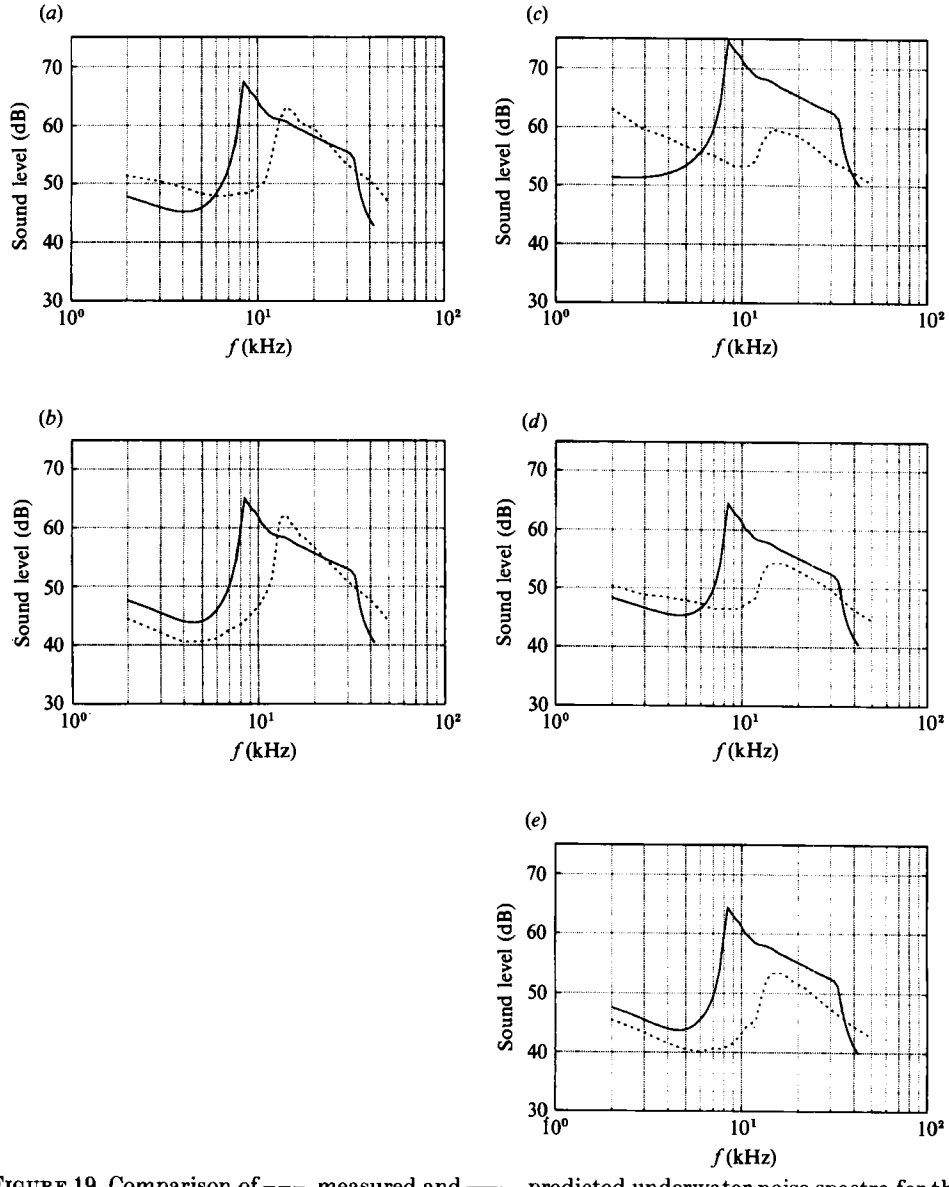

FIGURE 19. Comparison of – – –, measured and ——, predicted underwater noise spectra for the rain events of Scrimger *et al.* (1987). (*a*) Rainfall rate 0.4 mm/h, wind speed 0.9 m/s. (*b*) Rainfall rate 0.3 mm/h, wind speed 0.9 m/s. (*c*) Rainfall rate 3.2 mm/h, wind speed 1.4 m/s. (*d*) Rainfall rate 0.6 mm/h, wind speed 1.4 m/s. (*e*) Rainfall rate 0.4 mm/h, wind speed 1.4 m/s.

possible that drops impacting a disturbed surface entrain bubbles in a less predictable fashion than in the case of a quiescent surface, which would tend to blur the spectral peak. The model used in this paper is evidently incapable of accounting for these effects without the introduction of empirical probabilistic elements. Recent laboratory investigations also indicate that impacts at angles greater than 20°–30° from the normal inhibit bubble entrapment (Medwin 1990; Medwin, Kurgan & Nystuen 1990). Neglect of this fact would then result in an overprediction of the spectral level which could explain why, in our results, the theoretical levels for events

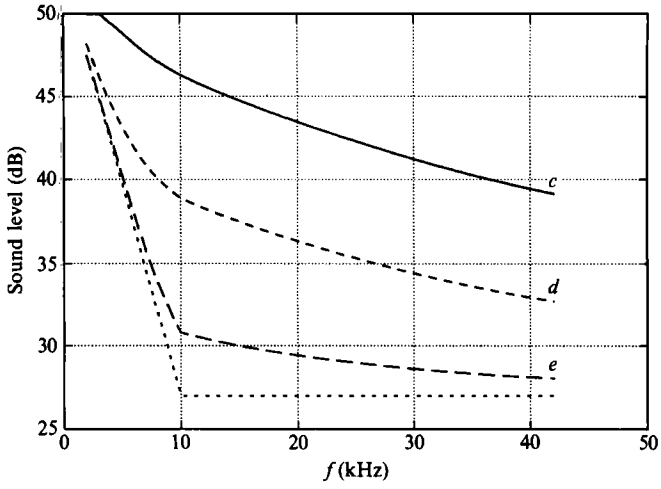

FIGURE 20. Calculated sound level spectrum of rain including only $\cdots$, background noise and impact noise for rain events *c* and *d* and *e* of Scrimger *et al.* (1987).

c and *e* are significantly larger than the experimental ones while for events *a* and *b* the two match within a few decibels.

The above considerations indicate that, as could be expected, a natural rain event is far more complex than the highly idealized model used in our calculations. In this respect, our procedure can certainly benefit from further work tending to make the model more realistic. At the same time, however, the model does suggest very strongly that the prominent peak in the spectrum of rain is due to the oscillations of entrained air bubbles. To further corroborate this interpretation, we show in figure 20 the sound levels predicted by neglecting bubble oscillations and including only the measured background noise (dotted line) and the impact mechanism of §5 for events *c*–*e*. It is obvious that, while matching with experimental data below a few kHz is possible, at higher frequencies noise levels many orders of magnitude lower than the observed ones are predicted by neglecting bubble emissions.

An immediate consequence of the mechanism of rain noise put forward in this paper is a scaling law for the underwater noise signature of rain. This can be seen as follows. Let us assume for simplicity that the raindrop number density $n(R)$ appearing in (5) can be approximated by a constant,

$$n(R) \approx \frac{N}{R_{\mathrm{M}}-R_{\mathrm{m}}}, \tag{31}$$

where N is the total number per unit area and time of bubble-entraining drops with radius in the range $R_{\mathrm{m}} \leqslant R \leqslant R_{\mathrm{M}}$. Then (2) can be re-written in the form

$$\log_{10}\frac{F(\omega)}{T[P^2_{\mathrm{ref}}/1\ \mathrm{Hz}]} = \log_{10}\left(10^{0.1\,SL}-\frac{|\hat{p}_{\mathrm{l}}|^2+|\hat{p}_{\mathrm{b}}|^2}{T[P^2_{\mathrm{ref}}/1\ \mathrm{Hz}]}\right)-\log_{10} n, \tag{32}$$

where F is a *universal function* defined by

$$F(\omega) = \int_{R_{\mathrm{m}}}^{R_{\mathrm{M}}} \frac{R_{\mathrm{b}} d}{c}|\hat{p}_{\mathrm{B}}|^2\,\mathrm{d}R, \tag{33}$$

with $\hat{p}$ given by (11).

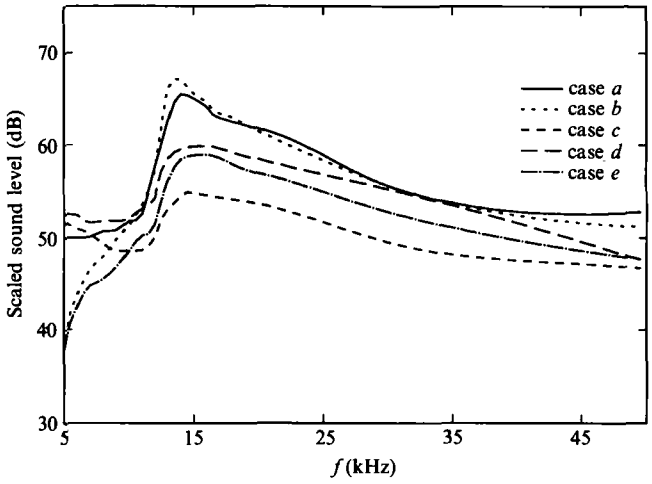

FIGURE 21. Underwater rain noise data of Scrimger *et al.* (1987) for rain events *a–e* scaled according to (32) with the drop count in the range 0.4–0.6 mm of drop radii.

The data of Scrimger *et al.* (1987) are replotted in figure 21 in the fashion suggested by this relation. It is seen that rain events *a* and *b* conform rather closely with this prediction, unlike the other ones. It is interesting to note that the curve corresponding to the highest rainfall rate, 3.2 mm/h (event *c*), when plotted in this way, lies below the other ones. As mentioned before, these circumstances may be due to an inhibition of the bubble entrainment mechanism in the presence of wind and surface disturbances. A further possible reason of the only limited success of the suggested scaling is the rather inaccurate estimate of the drop number in the narrow range of radii of interest. Clearly, better data are needed for a more stringent test of this hypothesis.

Finally, we show in figure 22 a graph of our computed value of the universal function F compared with the average of the five spectra of figure 21. The similarity between the two structures is quite striking.

7. Summary and conclusion

We have shown that available measurements of the underwater noise produced by rain cannot even remotely be explained in terms of the impact noise produced by rain drops hitting the surface of the receiving liquid. We have made an attempt to predict the observed noise on the basis of numerical calculations of bubble entrainment by drop impacts. The computed results show a broad agreement of the predicted sound levels and general shape of the spectral peak with experiments. However, the maximum of the peak appears to be centred at about 8 kHz rather than 14. The origin of this difference is unknown but is believed to be related to several errors and approximations in the calculation, on the one hand, and to the extreme sensitivity (demonstrated by experiments) of the entrainment process to even minute perturbations. In a related paper (Oğuz & Prosperetti 1990*d*) we have studied the sensitivity of the volume of the entrained bubble to the numerical dissipation used in the calculation. We have found that a slight increase of the latter with respect to the procedure used in the present calculations leads to larger bubbles. Hence the discrepancy between experimental and calculated results cannot be imputed to the

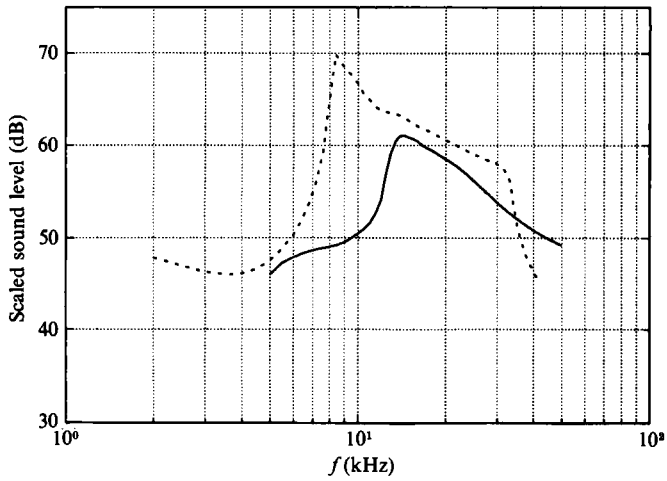

FIGURE 22. – – –, the universal function F defined by (33) compared with ——, the average of the five normalized spectra of figure 21.

dissipative surface smoothing techniques that we have used to stabilize the numerical calculation.

While it is evident that further refinements of our method would be desirable, we believe that the preceding results lend considerable support to the idea that bubble entrainment is responsible for the underwater noise of rain. Our purely theoretical argument in support of this mechanism complements the experimental indications obtained in the laboratory by Pumphrey, Crum, and co-workers. In a broader context, one would expect that entrained air would nearly always dominate underwater noise. An important example is furnished by the breaking of waves.

The recent finding that drops impacting at non-normal incidence are less likely to consistently entrain bubbles (Medwin 1990; Medwin *et al.* 1990) has motivated the hypothesis that ambient noise under agitated conditions should be attributed to the impact process (Nystuen 1990). Although the question must be left open at this time, on the basis of our results, we strongly doubt that impact can ever be a significant source of underwater noise. Other bubble-entraining processes (e.g. enhanced micro-breaking, local disruption of the surface vortical layer) are possible and may play a significant role under those conditions.

If the explanation of the prominent 14 kHz-peak of the underwater noise of rain put forward here is correct, it follows that its level is not correlated to the total amount of rainfall, but is only sensitive to the population of drops with diameters between 0.9 and 1.2 mm capable of entraining bubbles. Hence, other frequency ranges should be used for the acoustic monitoring of the total rainfall over bodies of water (Nystuen & Farmer 1989). Of course, in principle, the 14 kHz-peak could be used if the shape of the size distribution of drops were known, but this is unfortunately hardly ever the case.

The authors wish to express their gratitude to Dr Larry A. Crum and Dr Hugh C. Pumphrey for liberally sharing with them their data and observations. They are also indebted with Dr Joseph A. Scrimger for allowing them to reproduce his figures 8 and 9.

This study has been supported by the Ocean Acoustics Program of the Office of Naval Research.

REFERENCES

DETSCH, R. M. & HARRIS, I. A. 1990 Bubble entrainment by impacting drops in various liquid solutions. To be published.

DINGLE, A. N. & LEE, Y. 1972 Terminal fallspeeds of raindrops. *J. Appl. Met.* **11**, 877–879.

FRANZ, G. J. 1959 Splashes as sources of sound in liquids. *J. Acoust. Soc. Am.* **31**, 1080–1096.

LONGUET-HIGGINS, M. S. 1990 An analytic model of sound production by rain-drops. *J. Fluid Mech.* **214**, 395–410.

MEDWIN, H. 1990 Impact and bubble radiation from obliquely incident rain. In *Natural Physical Sources of Underwater Sound* (ed. B. R. Kerman). Reidel, in press.

MEDWIN, H., KURGAN, A. & NYSTUEN, J. A. 1990 Impact and bubble sound from raindrops at normal and oblique incidence. *J. Acoust. Soc. Am.* **88**, 413–418.

NYSTUEN, J. A. 1986 Rainfall measurements using underwater ambient noise. *J. Acoust. Soc. Am.* **79**, 972–982.

NYSTUEN, J. A. 1990 An explanation of the sound generated by light rain in the presence of wind. In *Natural Physical Sources of Underwater Sound* (ed. B. R. Kerman). Reidel, in press.

NYSTUEN, J. A. & FARMER, D. M. 1989 Precipitation in the Canadian Atlantic Storms Program: Measurements of the acoustic signature. *Atmos. Ocean* **27**, 237–257.

OĞUZ, H. N. & PROSPERETTI, A. 1990*a* Bubble entrainment by the impact of drops on liquid surfaces. *J. Fluid Mech.* **219**, 143–179.

OĞUZ, H. N. & PROSPERETTI, A. 1990*b* Bubble oscillations in the vicinity of a nearly plane free surface. *J. Acoust. Soc. Am.* **87**, 2085–2092.

OĞUZ, H. N. & PROSPERETTI, A. 1990*c* Bubble entrapment by axisymmetric capillary waves. In *Engineering Science, Fluid Dynamics, A Symposium to Honor Theordore Yao-Tsu Wu* (ed. G. T. Yates), pp. 191–202. World Scientific.

OĞUZ, H. N. & PROSPERETTI, A. 1990*d* Drop impact and the underwater noise of rain. In *Natural Physical Sources of Underwater Sound* (ed. B. R. Kerman), Reidel, in press.

PROSPERETTI, A. 1984 Bubble phenomena in sound fields. *Ultrasonics* **22**, 69–77.

PROSPERETTI, A. 1991 The thermal behaviour of oscillating gas bubbles. *J. Fluid Mech.* **222**, 587–615.

PROSPERETTI, A., PUMPHREY, H. C. & CRUM, L. A. 1989 The underwater noise of rain. *J. Geophys. Res.* **94**, 3255–3259.

PUMPHREY, H. C. 1989 Sources of ambient noise in the ocean: an experimental investigation. PhD dissertation, University of Mississippi.

PUMPHREY, H. C. & CRUM, L. A. 1988 Acoustic emissions associated with drop impacts. In *Natural Mechanisms of Surface-Generated Noise in the Ocean* (ed. B. R. Kerman), pp. 463–483. Reidel.

PUMPHREY, H. C. & CRUM, L. A. 1990 Free oscillations of near-surface bubbles as a source of the underwater noise of rain. *J. Acoust. Soc. Am.* **87**, 142–148.

PUMPHREY, H. C., CRUM, L. A. & BJØRNØ, L. 1989 Underwater sound produced by individual drop impacts and rainfall. *J. Acoust. Soc. Am.* **85**, 1518–1526.

PUMPHREY, H. C. & ELMORE, P. A. 1990 The entrainment of bubbles by drop impacts. *J. Fluid Mech.* **220**, 539–567.

RICHARDSON, E. G. 1948 The impact of a solid on a liquid surface. *Proc. Phys. Soc.* **61**, 352–367.

RICHARDSON, E. G. 1955 The sounds of impact of a solid on a liquid surface. *Proc. Phys. Soc.* **68**, 541–547.

SCRIMGER, J. A. 1985 Underwater noise caused by precipitation. *Nature* **318**, 647–649.

SCRIMGER, J. A., EVANS, D. J., MCBEAN, G. A., FARMER, D. M. & KERMAN, B. R. 1987 Underwater noise due to rain, hail and snow. *J. Acoust. Soc. Am.* **81**, 79–86.

SCRIMGER, J. A., EVANS, D. J. & YEE, W. 1989 Underwater noise due to rain – Open ocean measurements. *J. Acoust. Soc. Am.* **85**, 726–731.